Original Article

Identification of Circular Patterns in Capsule Endoscopy Bubble Frames

Abstract

Background: A significant number of frames captured by the wireless capsule endoscopy are involved with varying amounts of bubbles. Whereas different studies have considered bubbles as nonuseful agents due to the fact that they reduce the visualization quality of the small intestine mucosa, this research aims to develop a practical way of assessing the rheological capability of the circular bubbles as a suggestion for future clinical diagnostic purposes. **Methods:** From the Kvasir-capsule endoscopy dataset, frames with varying levels of bubble engagements were chosen in two categories based on bubble size. Border reflections are present on the edges of round-shaped bubbles in their boundaries, and in the frequency domain, high-frequency bands correspond to these edges in the spatial domain. The first step is about high-pass filtering of border reflections using wavelet transform (WT) and Differential of Gaussian, and the second step is related to applying the Fast Circlet Transform (FCT) and the Hough transform as circle detection tools on extracted borders and evaluating the distribution and abundance of all bubbles with the variety of radii. **Results:** Border's extraction using WT as a preprocessing approach makes it easier for circle detection tool for better concentration on high-frequency circular patterns. Consequently, applying FCT with predefined parameters can specify the variety and range of radius and the abundance for all bubbles in an image. The overall discrimination factor (ODF) of 15.01, and 7.1 showing distinct bubble distributions in the gastrointestinal (GI) tract. The discrimination in ODF from datasets 1–2 suggests a relationship between the rheological properties of bubbles and their coverage area plus their abundance, highlighting the WT and FCT performance in determining bubbles' distributions for diagnostic objectives. **Conclusion:** The implementation of an object-oriented attitude in gastrointestinal analysis makes it intelligible for gastroenterologists to approximate the constituent features of intra-intestinal fluids. this can't be evaluated until the bubbles are considered as non-useful agents. The obtained results from the datasets proved that the difference between the calculated ODF can be used as an indicator for the quality estimation of intraintestinal fluids' rheological features like viscosity, which helps gastroenterologists evaluate the quality of patient digestion.

Keywords: *bubble, small bowel, fast circlet transform, wireless capsule endoscopy, foam analysis, foam metrics, rheological features analysis*

**Hossein Mir[1],
Vahid Sadeghi[1],
Alireza Vard[1,2],
Alireza Mehri Dehnavi[1,2]**

[1]*Department of Bio-Electrics and Biomedical Engineering, School of Advanced Technologies in Medicine, Isfahan University of Medical Sciences,* [2]*Medical Image and Signal Processing Research Center, School of Advanced Technologies in Medicine, Isfahan University of Medical Sciences, Isfahan, Iran*

Introduction

In recent years, wireless capsule endoscopy (WCE) has rapidly developed as a novel technology for detecting gastrointestinal (GI) diseases.[1-3] The entire endoscopy examination usually lasts around 6–8 h, and if WCE takes real-time photos every 2 s, around 40–60 thousand frames will be generated. Due to the uncontrolled movements of the capsule through the GI tract, many frames with quality-reducing agents appear in the WCE video, which can lead to misdiagnosis.[4] Although not all frames are helpful, bubble-engaged ones with significant bubbles could contain useful information.

Aerated products include soap, crude oil, bread, beer, shaving cream, fire-fighting foams, and polyurethane insulating materials. These products can be classified as either foams or having been foams during processing.[1] Foams, which consist of gas bubbles surrounded by a liquid matrix, exhibit intricate flow properties. Their behavior is characterized by non-Newtonian and time-dependent properties, along with apparent boundary slip effects and compressibility. Researchers conducted various studies to measure the distribution of bubble sizes in foams, aiming to assess the rheological

Access this article online

Website: www.jmssjournal.net

DOI: 10.4103/jmss.jmss_50_23

Quick Response Code:

characteristics such as viscosity, stability, and draining. For example, viscosity, which is referred to the flow properties of foam, is influenced by the fluid properties and bubble geometry.[2] Higher viscosity can hinder bubble mobility and coalescence, causing smaller and more concentrated gas pockets. Conversely, lower viscosity enables bubbles to move and clump together more easily, resulting in larger and more scattered gas pockets and increases the mean size of bubbles.

Through various examinations, the distribution histogram and mean of measured radii for bubbles serve as indicators of the foam's rheological properties.[1,2,5] Du *et al*.'s research[6] highlighted the significance of bubble size in predicting protein separation and concentration in foam fractionation. Their work measures not only the interfacial area but also the coalescence of bubbles in foam. They present a photoelectric method that has been developed to measure the distribution of bubble sizes in both bubble and foam columns employed in protein concentration.

The rheological features of intraintestinal fluids, which are influenced by several factors, such as the composition of the mucus layer, the hydration status of the body, the presence of digestive enzymes and acids, and the activity of the intestinal epithelium, are a key factor in the number and size of created bubbles.[7] The effect of changing the rheological features in intraintestinal fluids is dependent on other factors, such as intestinal motility, luminal pressure, and bubble surface tension.[8-11] Therefore, bubble specification can help analyze the rheological features of intraintestinal fluids near captured frames in WCE videos for digestive approaches.

The bubbles in the GI tract are mainly caused by the combination of intraintestinal fluids and the ingestion of air (aerophagia) or the production of gas by the intestinal microbiota.[12] They are a combination of mucus, gas, bile, and come in quasi-circular shapes and multiple sizes as shown in Figure 1, accounting for 20%–30% of all captured frames. Thus, they may be one of the agents containing important information that should be detected from WCE video frames to enhance the diagnostic process or assessing cleanliness and digestion processes.[13-15]

Assessing and analyzing bubbles in the small bowel by humans is subjective and unreliable because of inaccessibility, but computer vision-based algorithms can enhance accuracy and objectivity in measuring bubbles in WCE images.[13] There are several approaches for identification these agents: morphological approaches, texture-based approaches, and color-based approaches. The morphological approaches aim the unique structure of bubbles in the WCE images. Bubbles in WCE images were distinguished by the ring shape selective (RSS) filters, which analyzed the bubbles' morphological properties. The images underwent conversion to grayscale and then an RSS filter was applied to accentuate the bubble areas. Using an optimal threshold, the filtered image output was converted to a black-and-white image. Finally, by applying various morphological operations like erosion, scattered small regions were removed.[16] The Gabor filter's potential to capture bubbles' structure is another way of detecting them in these approaches.[17] The capability of identifying the circular texture of bubbles is evaluated in texture-based approaches through computed techniques such as gray-level of co-occurrence matrix, fractal dimension, Hough transform (HT), and Speeded-Up Robust Features (SURFs).[3] Another technique for detecting bubble frames with color features is through color-based approaches. These works detected all bubble frames using a collaboration of local color histogram for colorful bubbles and Gauss–Laguerre Transform, for noncolorful bubbles.[4,18] In another study, the bubbles' color and texture features are extracted using the Color Local Binary Pattern algorithm with Discrete Cosine Transform.[19] Utilizing MPEG-7 dominant color descriptor is another technique to analyze color and texture features of bubbles.[20] In another proposed system, utilizing a two-stage system including identification and segmentation methods, initially, contaminated color frames were recognized by performing support vector machine (SVM) classification that relied on color histogram training. Next, the bubble frames were identified using the SURF texture descriptor.[21] In the recent study of Sadeghi *et al*.,[22] as part of the bubble boundary detection scheme, the sym10 wavelet was used to highlight the bubble regions. In their wavelet-based bubble edge detection trial, sym10 wavelet transform (WT) was selected because it enhances the highlighting of bubble edges. In the LL, HL, LH, and HH subbands (where L = low and H = high), the image
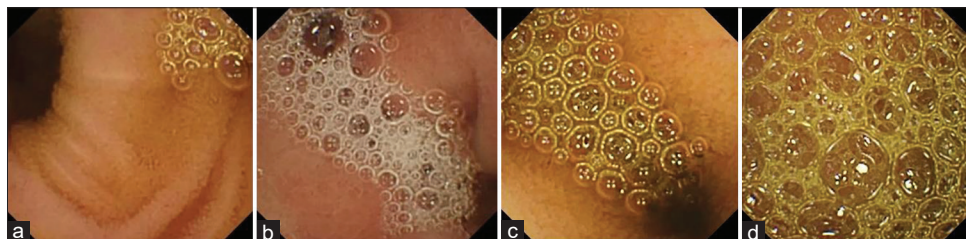
Figure 1: Bubble-engaged image examples with different abundance, colors, and size of bubble: (a) Low-level engagement of bubbles, (b) Low-level abundance of circular bubbles, (c) High-level abundance of circular bubbles, (d) High-level engagement of bubbles

was decomposed into four subbands in the first level. The original image was approximated by the LL subband, whereas the horizontal, vertical, and diagonal directions contain fine details in the other subbands. Then, the image's edges were improved by eliminating the LL subband of the second level, and they restored the spatial representation using the other subbands. Finally, the most expressive edges were discovered through their method.

Texture and shape-based methods were used to conduct multiple studies that aimed to exclude frames engaged with bubbles rather than evaluating them. The methods mentioned for detecting bubbles can only verify the presence of bubbles to classify the frame as a bubble-contaminated frame for exclusion from the WCE video in the pathological aims or for assessing the GI's cleanliness based on the total amount of bubbles for preparation paradigms. However, they do not offer positive insights into the circular patterns or size of the bubbles, whereas large bubbles may contain diagnostic regions, while small bubbles only reflect capsule light sources. Furthermore, the specification and separation of bubbles with different sizes from small to large can be a further crucial step in the estimation of intraintestinal fluids in WCE bubble-engaged frames. On the other hand, bubbles have visible borders and reflective properties that enable the distinguishability of high-frequency content. Frequency-based transforms are practical for filtering high-frequency contents, which are widely used in medical aspects for object detection.[23,24] To tackle the aforementioned challenges of conventional approaches, the potential of the Fast Circlet Transform (FCT) as one of the frequency-based transforms would be beneficial for identifying and separating circular bubbles from noncircular ones. FCT is a specific design of Wavelet and Curvelet Transforms that only capture the circular high-frequency patterns in the image.[25,26]

In the current work, by employing different preprocessing and circle detection methods like FCT and HT, our goal is to distinguish and detect circular bubbles in capsule endoscopy images and estimate their coverage area and number in an object-oriented manner. The method is presented as follows:
- Preprocessing
- Circle detection
- Bubble specification.

The paper's outline begins with a description of the used dataset, preprocessing approaches in extracting bubble borders, and FCT's performance on the preprocessed capsule endoscopy images with a predefined radius range and number of bubbles to be detected. Then, the coverage area and the abundance of bubbles for two different categories of bubble-engaged images are calculated. Finally, our method in determining the bubble distributions and their statistical features is compared to Differential of Gaussian (DoG) as a preprocessing method and the HT as a circle detection tool.

Materials and Methods

Datasets description

Dataset included capsule endoscopy bubble images which were selected from the Kvasir-capsule dataset that is available for download.[27,28] Using the Olympus Endocapsule system, SBCE videos were recorded and the images were saved in PNG and JPG format with 336 × 336 pixels resolution. The dataset we used consisted of 50 small bowel capsule endoscopy images, taken from various subjects and video sequences of SBCE.

To create two sets of bubble-engaged images, 25 images with small radius size were chosen for Dataset 1 and 25 images with highest possible radius size for Dataset 2. Bubbles with a wide variety of colors, sizes, and quantities were authorized and included by three different specialists in the image sets through a careful selection.

Figure 1 displays a few bubble-engaged images with varying degrees of contamination. In these frames, the surface of the mucosa cannot be visualized properly because it was covered with different amounts of air bubbles.

General Proposed framework

Bubbles can significantly reduce the visualization quality of the small bowel mucosa. Our main objective in this section was to find the best configuration of preprocessing and circle detector tools to evaluate the size and the number of circular bubbles in WCE frames for the discrimination of their distributions. Figure 2 provides an illustration of the general framework of this study. Initially, the image was preprocessed to distinguish the borders of the bubbles from the background tissue by focusing on high-frequency components. Following that, the circle detector tool was employed on the preprocessed image to determine bubble radii in an object-oriented manner. All images in each dataset were treated through this process. Finally, the distribution of bubbles was analyzed by calculating the coverage area and abundance of bubbles to understand their rheological features.

Preprocessing

Typically appearing round or oval, bubbles can have smooth or irregular boundaries and vary in size and aspect ratios. Depending on lighting conditions and surrounding tissue reflection, bubbles can appear in a range of colors, but they are usually white or light gray [Figure 1]. Identifying circular bubbles in capsule endoscopy video sequences could be an objective due to the diagnostic information they might contain. As bubbles are appeared in different shapes and aspect ratio, the response of frequency contents of bubbles varies. Bubbles that have a specific distribution of circular frequencies are crucial in FCT filters output. The reflection of capsule light emitters results in the reflection of borders appearing in a ring shape, which has diagnostic
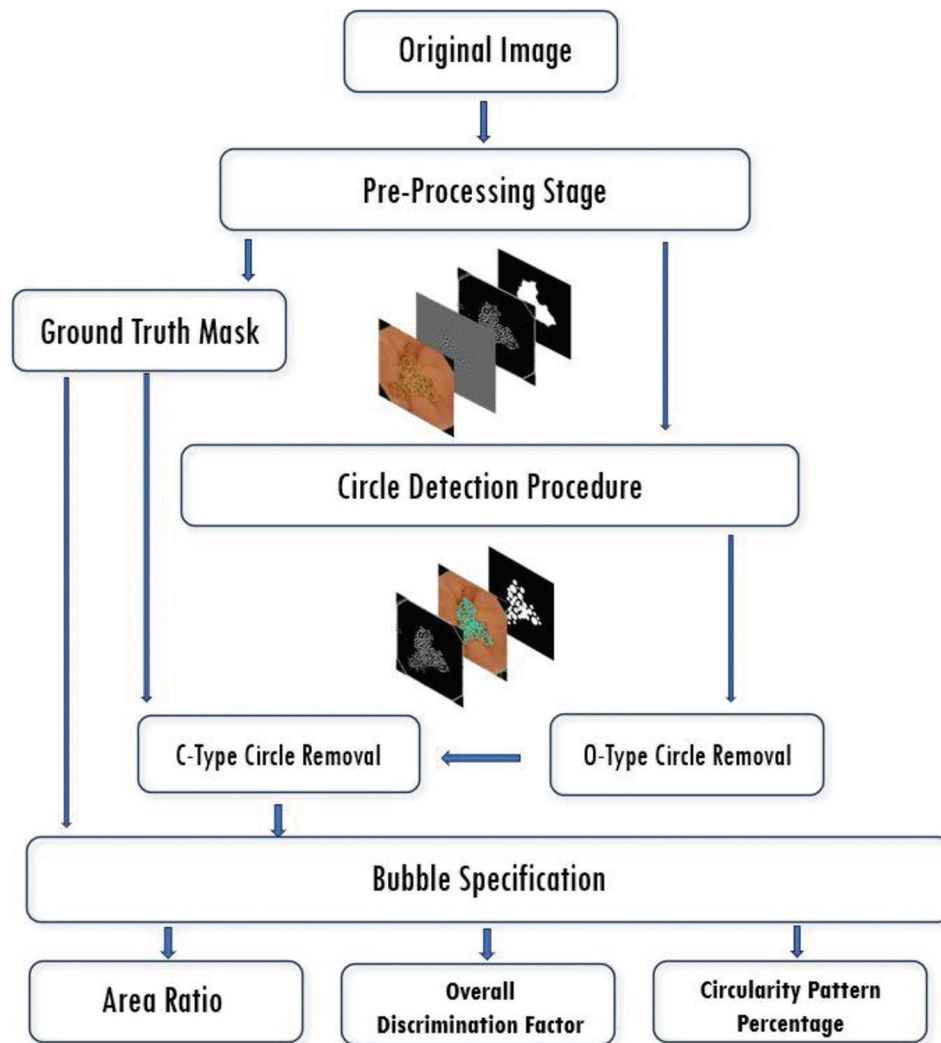
Figure 2: General framework of proposed method

information about the containing fluid. On the other hand, the bubble surface's ability to reflect light leads to surface reflections. The effectiveness of the bubble texture on these reflections is influenced by the quantity and type of fluid or air inside, which can make it either smooth or slightly rough. To achieve these regions, the DoG method and the two-dimensional discrete WT were used and the results were compared. In addition, using the morphological closing method, a ground truth mask is generated from the Otsu threshold image of each preprocessing method to assess the final results [Figure 3d].

Differential of Gaussian

The DoG technique is used in image processing to enhance image edges or gradients. The process entails subtracting one image with a higher blur level from another image with a lower blur level, achieved through the use of Gaussian filters with varying standard deviations. The image obtained highlights the areas where there are rapid changes in intensity, such as edges, corners, or blobs Figure 3b and c.[29]

Two-dimensional discrete wavelet transform

Oscillating wave-like functions called wavelets represent the mother wavelet in scaled and shifted versions.[30] An image can be decomposed into different frequency components at multiple resolutions using many wavelet filters.[31]

The bubble segmentation procedure was repeated to visually compare all candidates and determine the optimal mother wavelet function and wavelet decomposition level. To ascertain the best decomposition level and mother wavelet function, the experiment was conducted in two stages.

At the beginning of decomposition, the image is split into four subbands: LL, HL, LH, and HH subbands (L = low, H = high) Figure 4b. The LL subband is an approximation of the original image, while the other subbands capture fine details in different directions. Only the approximation subband (LL) undergoes further decomposition at each subsequent level in the higher level of decomposition.

Enhancing the edges of the image involves removing the LL subband from each level of decomposition and reconstructing the spatial representation using the remaining subbands [Figure 4c]. By using this method, the most expressive edges were found [Figure 4d]. The selection of Level 3 in our wavelet-based bubble edge detection trial was based on its ability to highlight bubble edges more effectively.

Empirical results suggest that the "sym10" from the Symlets family is the most suitable mother wavelet function.

Finally, using the Otsu algorithm, all bubble regions were obtained in a binary image.

Circle detection

Hough transform

The HT is a technique for detecting incomplete and overlapping geometric shapes, like lines, ellipses, and circles, despite noise, using a voting procedure in the parameter space.[32]

The Canny edge detector can be used to detect prominent edges as a preprocessing stage.[33] The circular HT algorithm effectively detects highly radially symmetrical objects. The centroid coordinates and radius of circular patterns in an image can be obtained by utilizing a 3-dimensional Hough search space. To locate circles of an unknown radius, a circular HT can search a triplet transform space using the circle center coordinates and radius range as dimensions.[3] In our circular Hough trial, radius values and center locations of bubbles have been calculated to compare the circle detectors' performance with the other one.

The Fast Circlet Transform

Chauris *et al.*[25] first introduced the FCT, which is a robust tool for circular object detection in an image. This method has the highest similarity either conceptually or practically in the Curvelet transform,[34,35] doesn't need any segmentation methods, and doesn't need image binarization accordingly. Using a series of fast Fourier transform, this method decomposes any $f(x,y)$ gray-scaled image into band-limited circles called circlets with different radius in spatial domain and certain frequency contents in the frequency domain. Eqs. 1 and 2 indicate this decomposition in spatial domain with the associated amplitudes of A_λ:

$$f(x,y) = \Sigma_\lambda A_\lambda . c_\lambda(x,y) \tag{1}$$

$$A_\lambda = <f, c_\lambda> = \int \int f(x,y) . c_\lambda(x,y)\, dxdy \tag{2}$$

In the equations above, $\lambda = (x_0, y_0, r_0, f_0)$ serves as a characterization parameter for each c_λ, which represents the detected circlet with specific characteristics. These circlets are generated by modifying a basic circlet c_{ref} through shifts in position of centers (x_0, y_0), changes in radius (r_0), or the central frequency (f_0). Eq. 3 shows the circlet function:

$$c_\lambda(x,y) = \Omega[2\pi f_0(r - r_0)] \tag{3}$$

Where $r = \sqrt{(x - x_0)^2 + (y - y_0)^2}$ is radius of circlets and Ω is an oscillating function, such as wavelet function, to mirror the oscillating features of circular patterns in the frequency domain. The 1D filter banks or oscillating function $F_k(\omega)$ oscillates between positive and negative values at different frequencies (defined in Eq. 4) and used for creating the 2-dimensional filter banks $G_k(\omega_1, \omega_2)$ which represent circular patterns in the frequency domain:

$$F_k(\omega) = \begin{cases} cos(\omega \pm \omega_k); & |\omega \pm \omega_k| \le \dfrac{\pi}{N-1} \\ 0; & otherwise \end{cases} \tag{4}$$

Where N is the number of band limited filters, k is a controlling parameter for frequency contents of circlets $(k = 1,\ldots, N)$, and $\omega_k = \dfrac{\pi(k-1)}{N-1}$

There are also two rules which are needed for reconstructing an image perfectly:

$$\Sigma_k |F_k(\omega)|^2 = 1, \Sigma_k |G_k(\omega_1, \omega_2)|^2 = 1 \tag{5}$$

The $F_k(\omega)$ along the circumference of a circle with a certain width creates the circlet function. To cover different radius range of circular patterns, a phase delay needs to be considered as (6) with $\omega = (\omega_1, \omega_2)$ and $|\omega| = \sqrt{\omega_1^2 + \omega_2^2}$:

$$G_k(\omega) = e^{i|\omega|\ell} . F_k(|\omega|) \tag{6}$$

In the Fourier domain, the distance of the frequency component from the origin is represented by the magnitude of the complex number $|\omega|$. The term $e^{i|\omega|\ell}$ function is to adapt the oscillating function for detecting circular patterns at a specific radius of r_0. By varying radius of r_0 by $\ell = 1,\ldots,M$ (M is the total number of radii to be detected by FCT) in the Eq. 6, filters $G_k(\omega_1, \omega_2)$ which act as the reference circlets, will be able to detect the objects with different sizes. The detected circles which are in frequency domain are obtained from Eq. 7:

$$\hat{c}_{lk}(\omega) = e^{i<\omega, x_c>} . G_k(\omega), \text{for } \{k = 1, \ldots, N\} \text{ and}$$
$$r_0 = \ell = \{1,\ldots,M\} \tag{7}$$

In the context of FCT, to detect circular patterns locally, the term $e^{i<\omega, x_c>}$ combines frequency content (ω) and central position (x_c) in the Fourier domain with phase modulation. Capturing circular structures at specific positions, orientations, and scales is an essential part of the FCT process.

Focusing on bubbles is easier for the FCT by extracting bubble borders as high-frequency components in the preprocessing stage. This allows segregation of only circular patterns from noncircular ones by applying FCT on extracted border regions. On the other hand, one of the main problems of FCT is false detection of bubbles. Overlapped circles (O-type circles) are the ones inside a bigger circle. There are also some conflict circles (C-type circles) that do not represent any meaningful circular

objects in an image. These kinds of detected circles affect the estimation of bubble distribution in the image, so they should be removed from the output of FCT.

False circle removal

To remove the unintentional circles for more accurate estimation of bubble distributions, we discarded any circles with centers closer than the largest radius. Moreover, the ground truth mask obtained during preprocessing was used to eliminate any bubbles detected outside the bubble region, resulting in the removal of all centers outside the ground truth mask. The total number of remaining bubbles, which represent their abundance, were only those within the bubble region of the ground truth image, with no additional circles inside, and can be derived from the Eq. 8:

$$\eta_t = N - \eta_0 - \eta_c \tag{8}$$

Where the N is the total number of circles as an input parameter for FCT, η_0 the number of O-type circles, and η_c is the number of C-type circles outside of the white regions in ground truth mask.

Bubble specification

This section represents all calculations related to the bubbles including automatic and semiautomatic methods, and it serves as a circular feature extractor of bubbles. The radius mean, dice similarity coefficient (DSC), area ratio (AR), and overall discrimination factor (ODF) are automatic evaluation metrics. The circularity patterns percentage (CPP) is a semi-automatic evaluation metric.

Semiautomatic evaluation metrics: Circularity patterns percentage

Visually assessable, the CPP validates detected circular bubbles against all bubbles including circular and noncircular ones. This value is calculated for the dataset j in the Eq. 9:

$$CPP_j = \frac{\sum_{i=1}^{k} \dfrac{n_{ij}}{N_{ij}}}{k} \tag{9}$$

Where the i refers to each image, n_{ij} is the visually truly detected circular bubbles by FCT, N_{ij} is the total number of bubbles that are counted by specialists, and k is the total number of images in the dataset j. This value is the benchmark for evaluating the circle detector tool compared to the preprocessing approaches, so strong detection is very crucial in its measuring. By involving third-party specialists to count the total number of bubbles in the image in the observatory and trial-and-error attempts by changing FCT parameters, the algorithm becomes semiautomatic and time-consuming. This parameter, which is obtained by supervised calculations, will be used to compare to automatic evaluation metrics.

Regarding the experience of applying FCT as a software caliper on the preprocessed images of datasets with different trials on different radius ranges, and calculating radius histograms of detected bubbles [Figure 5], an initial radius size (r_0) of 5–30 with $N = 50$ has been chosen as an input parameter for FCT to compute automatic evaluation metrics.

Automatic evaluation metrics

The AR is a factor that assesses coverage of detected circles using FCT compared to the ground truth mask, particularly when precise overlap with ground truth is less significant than DSC. This value is derived from the Eq. 10:

$$AR_j = \frac{\sum_{i=1}^{k} \dfrac{Area_{FCT}(i)}{Area_{groundtruth}(i)}}{k} \tag{10}$$
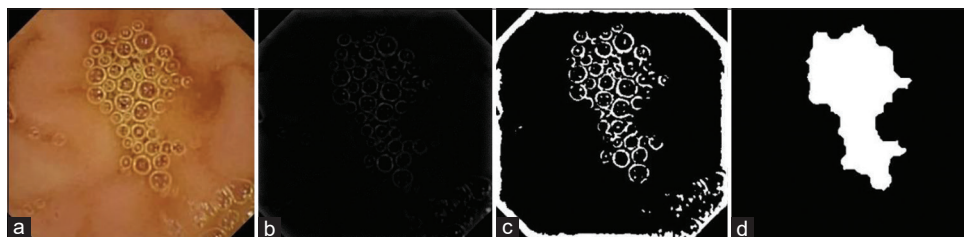

Figure 3: Extracting borders using Differential of Gaussian (DoG): (a) Original image, (b) DoG filtered image, (c) Otsu thresholding of filtered image, (d) Created mask using morphological closing

Figure 4: A decomposed image with three-level "sym10" wavelet transform (WT). (a): Original image, (b): Three levels of decomposition in the two-dimensional discrete WT, (c): Transform modified by zeroing the LL subband, (d): Reconstructed edge image

Where the $Area_{FCT}(i)$ is the white area of truly detected bubbles mask of the image i in the dataset j with k images, and $Area_{groundtruth}(i)$ is for the ground truth mask.

The number of truly detected bubbles using FCT is related to AR through the evaluation method known as the ODF. Eq. 11 is used to calculate this value, which is important for the classification and scaling of bubble distributions based on their coverage area and abundance (η_t).

$$ODF_j = \frac{\sum_{i=1}^{k} \eta_t(i) \times \dfrac{Area_{FCT}(i)}{Area_{groundtruth}(i)}}{k} \tag{11}$$

This value will not need initial supervision when it comes to comparison with CPPs. Therefore, if the input parameters are accurate, it can be a precise estimation of bubble distribution.

Implementation Results

This section represents the quantitative and qualitative diagnostic capability of FCT in finding bubbles.

Figure 6 depicts the false bubbles types and their removal after applying FCT as a postprocessing step.

Figure 7 shows the results of applying FCT on extracted borders of bubbles using the WT-FCT based method.
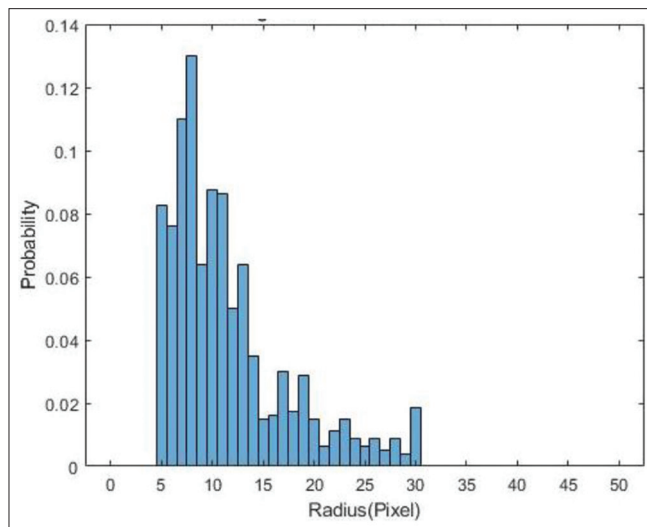

Figure 5: Histogram of detected initial radius range for wavelet-based approach using Fast Circlet Transform
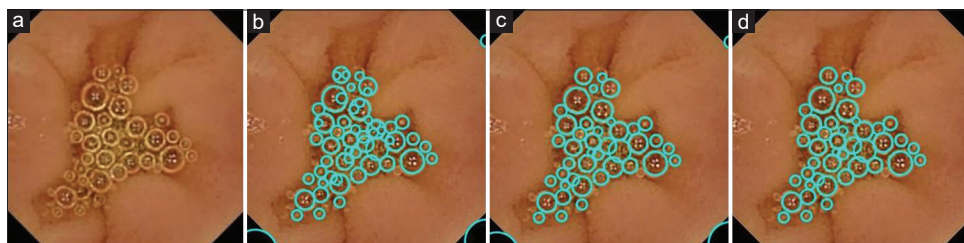
Table 1 presents the statistical calculations of all detected radii for distinguishing detected bubbles across different datasets. The CPP values were calculated for the best performance of the implemented methods for better comparison.

Figure 8 showcases the ODF metrics for different methods and highlights the best way to distinguish bubbles using the difference in overlapping standard deviations.

Evaluation of the Method Generalization Capability

To assess how the best-proposed method works on new data, or how much it is generalized, we implemented a Repeated-Stratified k-fold cross-validation (with the number of repeats 6) and computed different classification metrics like accuracy, precision, specificity, recall (sensitivity), and F1-Score [Table 2]. The dataset was divided into 3 folds where 2 folds were used to train the logistic regression, SVM, Naïve Bayes, and linear discriminant analysis as the classifiers. The remaining fold was used for testing the models and the procedure was repeated 6 times for better and balanced training of classifiers. Furthermore, to ensure a better comparison between artificial intelligence and machine learning methodologies, a straightforward multilayer perceptron network was utilized, featuring three primary layers (64 and 32 neurons with RELU activation function in the first and second layers, and one neuron with sigmoid activation function in the third layer). Labeling of the dataset was based on CPP values, where the large change between them was a good reference for labeling. Figure 9 provides the comparison of classifiers by the receiver operating characteristic curve and area under the curve.

Discussion

Our technique, which is based on the number and coverage of circular patterns in an object-oriented level, enables us to estimate the overall distribution of bubbles automatically in two different size-based WCE datasets using the FCT as a circle detector tool.

Our attitude differs from prior studies as it enables the detection and measurement of bubbles in every WCE frame, along with an approximation of their coverage area and abundance, in contrast to binary or multiclass classification on a frame-by-frame basis.
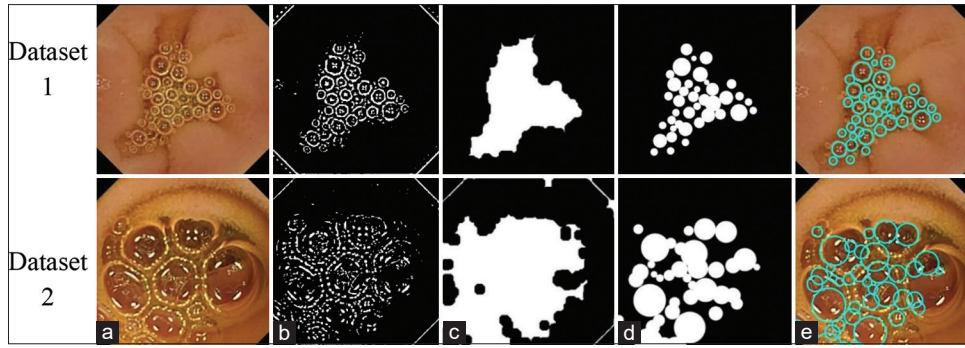

Figure 6: False circle removal: (a) Original image, (b) Initial detection of bubbles, (c) O-type circle removal, (d) C-type circle removal

Figure 7: Use implementation results instead of the selected words: (a) Original RGB image occupied by bubbles with different varieties of radius size, (b) Extracted reflection borders by wavelet transform, (c) Ground truth mask, (d) Fast Circlet Transform (FCT) mask, (e) Detected bubbles using FCT
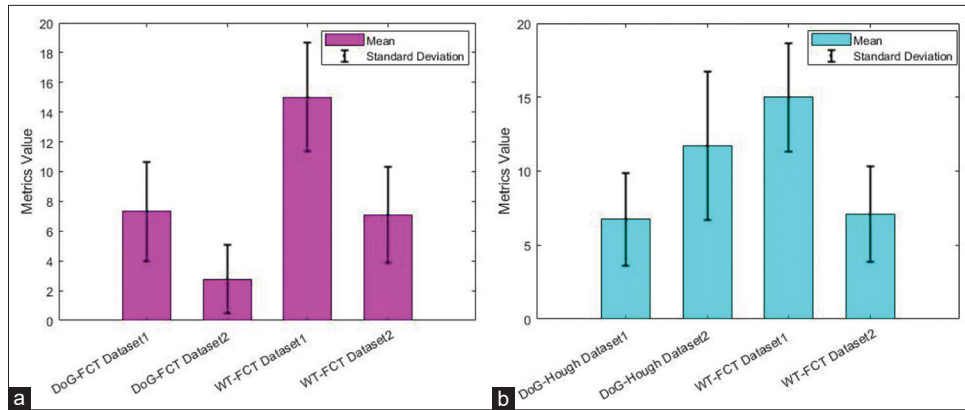

Figure 8: Graph representation of overall discrimination factor metrics: (a) Fast Circlet Transform (FCT), (b) Comparison of Hough transform and FCT performance. DoG – Differential of Gaussian, FCT – Fast Circlet Transform, WT-FCT – Wavelet transform FCT

Table 1: The quantitative distribution of detected bubbles for the Hough and Fast Circlet Transforms

	Mean	AR	DSC	ODF	CPP
HT					
Preprocessing method: DoG					
Dataset 1	8.5±3.95	0.3±0.06	0.3±0.05	6.74±3.13	
Dataset 2	7.01±4.2	0.35±0.12	0.27±0.04	11.71±5	
Preprocessing method: WT					
Dataset 1	10.6±6.24	0.03±0.12	0.36±0.11	6.45±3.1	
Dataset 2	6.87±1.8	0.26±0.11	0.24±0.6	6.25±4.02	
FCT					
Preprocessing method: DoG					
Dataset 1	12.88±4.72	0.36±0.11	0.35±0.7	7.32±3.35	
Dataset 2	9.00±7.42	0.3±0.17	0.17±0.06	2.78±2.28	
Preprocessing method: WT					
Dataset 1	13.41±5.22	0.47±0.98	0.57±0.61	15.01±3.66	88.44±8.25
Dataset 2	10.21±7.27	0.46±0.14	0.37±0.06	7.1±3.23	12.87±11.87

HT – Hough transform; FCT – Fast Circlet Transform; WT – Wavelet transform; DoG – Differential of Gaussian; AR – Area ratio; DSC – Dice similarity coefficient; ODF – Overall discrimination factor; CPP – Circularity patterns percentage

The quality of captured frames [Figure 7a] and detected border reflections greatly affects the performance of the circle detector in bubble detection and the creation of the ground truth mask [Figure 7c] through the preprocessing approach. Border reflections that are not strong and continuous enough against the regular tissue background can result in bubbles being missed in frames, because they do not share any circular patterns to be detected by circle detector tool. These reflections are predominantly observed in larger bubbles, resulting in a higher likelihood of missing their detection as high-frequency components using the circle detector [Figure 7 dataset 2].

The uncontrollable and inappropriate lighting conditions in the endoscopic capsule rendered high-pass filters like DoG

Table 2: Generalizability results of the presented method for the wavelet transform - Fast Circlet Transform approach

	Accuracy	Precision	Recall	F1-score	Specificity
SVM	0.89±0.07	0.87±0.09	0.92±0.08	0.89±0.06	0.86±0.11
Logistic regression	0.89±0.06	0.88±0.08	0.92±0.08	0.9±0.06	0.87±0.09
NB	0.82±0.08	0.83±0.1	0.84±0.11	0.82±0.07	0.8±0.13
LDA	0.86±0.09	0.85±0.08	0.88±0.15	0.86±0.11	0.85±0.11
KNN	0.89±0.06	0.88±0.08	0.92±0.06	0.9±0.06	0.87±0.09
MLP	0.9±0.06	0.89±0.08	0.92±0.08	0.9±0.06	0.87±0.1

SVM – Support vector machine; NB – Naïve Bayes; LDA – Linear discriminant analysis; MLP – Multilayer perceptron; KNN – K-Nearest Neighbors

ineffective in detecting bubbles. The preprocessed image underwent the circle detection procedure like HT and FCT, and the accuracy of the identified bubbles [Table 1] was assessed. There is a shared overlap of detected circles in the calculated standard deviations for some metrics in Table 1 and Figure 8 across each method. The lower overlapping of ODFs indicates the more differentiating of bubbles in detection procedure. Due to the limitations of the DoG method in uniformly differentiating bubble borders, losing a substantial number of detections, and inaccurately estimating bubble sizes in datasets, wavelets proved to be a more effective preprocessing method by sharing the less overlapping of detected bubble sizes [Figure 8a]. Furthermore, the large overlapping of the calculated ODF's standard deviations for DoG and HT implementation with 6.74 ± 3.13 for dataset 1 and 11.71 ± 5 for dataset 2 [Figure 8b and Table 1] indicates the inability of the HT in discrimination of large bubbles from small ones.

By collaborating FCT and WT, the stronger bubbles can be discriminated based on their size of round reflections, allowing for an approximate estimation of bubble coverage area in each image [Figure 7b and c]. According to Figure 7b and Table 1 for dataset 1, extracted borders produced stronger detection results by FCT due to the fact that they contain more continuous and circular patterns. Dataset 1 showed ODF results of 15.01 ± 3.66, while the second dataset had results of 7.1 ± 3.23. The absence of overlapping standard deviations allowed for more accurate bubble discrimination. This discrimination is decisive when compared to the significant discrimination of CPP values as a reference measure (88.44 ± 8.25 for dataset 1 and 12.87 ± 11.87 for the second dataset).

The continuity and circularity of border reflections are reduced as the size of bubbles increases. Consequently, the decrease in continuity and circularity patterns of borders results in a decrease in the accuracy of circle detection tools, causing false detection of bubbles in terms of size and location. This issue is quantified by decreasing of AR and ODF of detected bubbles from dataset 1–2 in Table 1. Therefore, the lower AR and ODF is a factor of circle detector inability to find bubbles based on their border reflections. The AR and ODF values will be the maximum for small bubbles due to the fact that they share uniform circular reflections and higher frequency response for applying FCT.

The number of truly detected bubbles (η_t) as the abundance plays a critical role in distinguishing small bubbles from large ones in frame-by-frame rheological analysis. The significance of this problem increases when the FCT is incapable of isolating each bubble at the object-oriented level, leading to inaccurate circle detection in the image. This causes false radius size and center locations for circles and consequently inaccurate calculation for all AR, η_t and ODF.

Our method improves the discrimination of bubbles and estimates their overall abundance by directly affecting ODF through AR and η_t, achieved by separating truly detected bubbles from C-type and O-type ones with the assistance of the ground truth mask [Eq. 11].

In the results of FCT implementation, the coverage area of detected bubbles [Figure 7d] and the truly detected number of bubbles (η_t) are the important features that represent the rheological properties of bubbles and foams. Consequently, to achieve better understanding of bubbles' properties, different distributions of bubbles' radii in datasets are quantified by calculating the mean, AR, and ODF values for all coverage area of each bubble engaged frames [Table 1], where bigger bubbles caused lower radii mean, lower AR and ODF, and small ones resulted higher AR, ODF, and higher mean radius.

These distributions indicate the existence of intraintestinal fluids in the frame with specific properties. The difference and discrimination of the calculated means and ODF as a function of AR and η_t between the datasets could be a good indicator of examining the rheological features of intraintestinal fluids like viscosity. Therefore, bubble specification can help analyze the rheological features of intraintestinal fluids near captured frames in WCE videos for digestive approaches.

By analyzing Figure 9 and Table 2, it is clear that there is a strong correlation between ODFs and CPPs, supporting the CPP usage as reference measures for evaluating automatic methods. By using our proposed method, we can distinguish the maximum number of circular patterns from noncircular ones and represent their distributions using ODF as a novel metric. The ODF's calculation method is currently a novel automated measurement approach to CPP values and is a viable option for use in the foam assessment field.
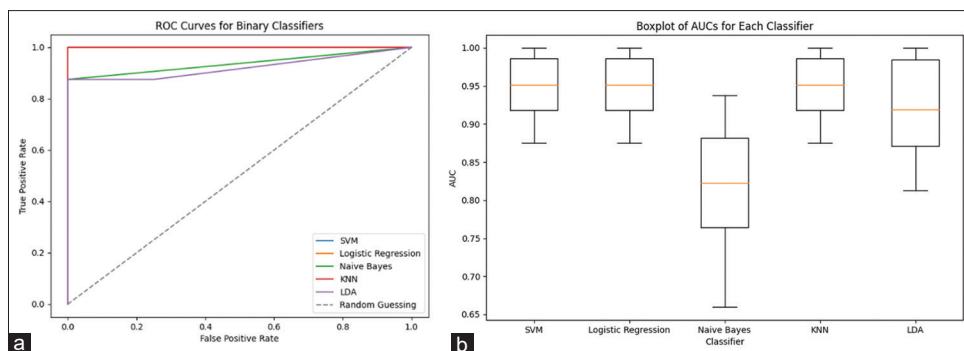
Figure 9: Classification plots of overall discrimination factor data: (a) Receiver operating characteristic curve, (b) Area under the curve boxplot. ROC – Receiver operating characteristic, AUC – Area under the curve, SVM – Support vector machine, LDA – Linear discriminant analysis, KNN – K-Nearest Neighbors

Conclusions

This manuscript used the potential of circular features of bubbles and provides a quantitative and qualitative representation of overall bubble distributions in the WCE bubble-engaged images as a proposed prerequisite step for future studies of intraintestinal properties. The collaboration of high-pass filtering method like WTs and a circle detection tool like FCT provides a better understanding of bubble structures as high-frequency components. Despite its success in detecting circles and capturing high-frequency circular components, FCT's weakness in detecting large bubbles and segregating individual bubbles in an object-oriented manner poses a significant obstacle to accurate bubble estimation. Our method of determining the number of truly detected bubbles and using it as an evaluation factor (named ODF) made it possible to discriminate the bubbles based on their covering area (AR) and abundance (η_t).

The object-oriented attitude toward bubbles makes it possible for them to be treated as useful agents in WCE images instead of contaminating agent assumption. The circularity features of bubbles provide a better understanding of the factors involving in creating bubbles. Therefore, evaluating the coverage area and abundance distributions in different GI parts or patients can assist gastroenterologists in achieving a more precise diagnosis based on the rheological features of intraintestinal fluids, ultimately aiding in evaluating patient digestion quality in future studies. This study, as a proposal for future studies, also requires more analysis to improve the results to reach the CPP results as a reference measure.

Acknowledgment

The authors' thanks go to all resource persons who were involved in any way in all stages of this research.

Conflicts of interest

There are no conflicts of interest.

References

1. Bisperink CG, Ronteltap AD, Prins A. Bubble-size distributions in foams. Adv Colloid Interface Sci 1992;38:13-32.
2. Calvert JR, Nezhati K. Bubble size effects in foams. Int J Heat Fluid Flow 1987;8:102-6.
3. Pietri O, Rezgui G, Histace A, Camus M, Nion-Larmurier I, Li C, *et al*. Development and validation of an automated algorithm to evaluate the abundance of bubbles in small bowel capsule endoscopy. Endosc Int Open 2018;6:E462-9.
4. Bashar MK, Kitasaka T, Suenaga Y, Mekada Y, Mori K. Automatic detection of informative frames from wireless capsule endoscopy images. Med Image Anal 2010;14:449-70.
5. Isarin, Jan-Cor, Antonie DJ Kaasjager, and Ronald BM Holweg. Bubble size distribution during the application of foam to fabrics and its effects on product quality. Textile research journal 1995; 65.2:61-69.
6. Du L, Ding Y, Prokop A, Tanner RD. Measurement of bubble size distribution in protein foam fractionation column using capillary probe with photoelectric sensors. Appl Biochem Biotechnol 2001;91-3:387-404.
7. Bonis V, Rossell C, Gehart H. The intestinal epithelium-Fluid fate and rigid structure from crypt bottom to villus tip. Front Cell Dev Biol 2021;9:661931.
8. Jia H, Zhang P. Bubble formation in viscous fluids by a microfluidic flow-focusing junction: A computational study. Microfluid Nanofluidics 2020;24:1-16.
9. Hlawitschka HW, Kováts P, Dönmez K, Zähringer H, Bart J. Bubble motion and reaction in different viscous liquids. Exp Comput Multiph Flow 2022;4:26-38.
10. Lin X, Bao F, Tu C, Yin Z, Gao X, Lin J. Dynamics of bubble formation in highly viscous liquid in co-flowing microfluidic device. Microfluid Nanofluidics 2019;23:1-9.
11. Oratis AT, Bush JW, Stone HA, Bird JC. A new wrinkle on liquid sheets: Turning the mechanism of viscous bubble collapse upside down. Science 2020;369:685-8.
12. Herath M, Hosie S, Bornstein JC, Franks AE, Hill-Yardin EL. The role of the gastrointestinal mucus system in intestinal homeostasis: Implications for neurological disorders. Front Cell Infect Microbiol 2020;10:248.
13. Houdeville C, Leenhardt R, Souchaud M, Velut G, Carbonell N, Nion-Larmurier I, *et al*. Evaluation by a machine learning system of two preparations for small bowel capsule endoscopy: The BUBS (burst unpleasant bubbles with simethicone) study.

J Clin Med 2022;11:2822.

14. Ponte A, Pinho R, Rodrigues A, Carvalho J. Review of small-bowel cleansing scales in capsule endoscopy: A panoply of choices. World J Gastrointest Endosc 2016;8:600-9.

15. Suman S, Hussin FA, Walter N, Malik AS, Hilmi I. Automatic detection and removal of bubble frames from wireless capsule endoscopy video sequences. Int Conf Intell Adv Syst ICIAS 2016. doi: 10.1109/ICIAS.2016.7824091.

16. Wang Q, Pan N, Xiong W, Lu H, Li N, Zou X. Reduction of bubble-like frames using a RSS filter in wireless capsule endoscopy video. Opt Laser Technol 2019;110:152-7.

17. Spyridonos P, Pujol O, Vitri J, Radeva P, Vall H. Automatic Detection of Intestinal Juices in Wireless Capsule Video Endoscopy. 2006. p. 18-21.

18. Bashar MK, Mori K, Suenaga Y, Kitasaka T, Mekada Y. Detecting informative frames from wireless capsule endoscopic video using color and texture features. Med Image Comput Comput Assist Interv 2008;11:603-10.

19. Sun Z, Li B, Zhou R, Zheng H, Meng MQ. Removal of non-informative frames for wireless capsule endoscopy video segmentation. IEEE Int Conf Autom Logist ICAL 2012:294-9. doi: 10.1109/ICAL.2012.6308214.

20. Bejakovic S, Kumar R, Member S, Dassopoulos T, Hager G. Analysis of Crohn's disease lesions in capsule endoscopy images, Proc IEEE Int Conf Robot Autom. 2009:pp. 2793-2798, doi: 10.1109/ROBOT.2009.5152774.

21. Seguí S, Drozdzal M, Vilariño F, Malagelada C, Azpiroz F, Radeva P, *et al.* Categorization and segmentation of intestinal content frames for wireless capsule endoscopy. IEEE Trans Inf Technol Biomed 2012;16:1341-52.

22. Sadeghi V, Vard A, Sharifi M, Mir H, Mehridehnavi A. Segmentation and region quantification of bubbles in small bowel capsule endoscopy images using wavelet transform. Inform Med Unlocked 2023;42:101364.

23. Kumar K, Mustafa N, Li JP, Shaikh RA, Khan SA, Khan A, Image edge detection scheme using wavelet transform, 2014 11th International Computer Conference on Wavelet Actiev

Media Technology and Information Processing (ICCWAMTIP), Chengdu, China, 2014:pp. 261-265. doi: 10.1109/ICCWAMTIP.2014.7073404.

24. Lama KN, Moustapha BM, Ali T, Lama KN, Moustapha BM, Ali T. White blood cells detection using spectral tresholding. J Signal Inf Process 2023;14:1-8.

25. Chauris H, Karoui I, Garreau P, Wackernagel H, Craneguy P, Bertino L. The circlet transform: A robust tool for detecting features with circular shapes. Comput Geosci 2011;37:331-42.

26. Liu H, Chen Z, Chen X, Chen Y. Multiresolution medical image segmentation based on wavelet transform. Conf Proc IEEE Eng Med Biol Soc 2005;2005:3418-21.

27. Vajira Thambawita HB, Riegler M, Hicks S, Halvorsen P, de Lange T, Smedsrud PH. The Kvasir-Capsule Dataset OSF; 2020. Available from: https://osf.io/dv2ag/. [Last accessed on 2020 Mar 13].

28. Smedsrud PH, Thambawita V, Hicks SA, Gjestang H, Nedrejord OO, Næss E, *et al*. Kvasir-capsule, a video capsule endoscopy dataset. Sci Data 2021;8:142.

29. Gonzales RC, Woods RE. Digital Image Processing Third Edition, 2021. [Online]. Available: http://localhost:80/xmlui/handle/123456789/428. [Last accessed on 2024 Feb 28].

30. Mallat SG. A Wavelet Tour of Signal Processing. Ukraine: Elsevier Science; 1999:p. 637.

31. Antoine JP, Murenzi R, Vandergheynst P, Ali ST. Two-Dimensional Wavelets and their Relatives. Cambridge University Press; 2004.

32. Illingworth J, Kittler J. A Survey of The Hough Transform. Comput Vision Graph Image Process 1988;44:87-116.

33. Canny J. A computational approach to edge detection. IEEE Trans Pattern Anal Mach Intell 1986;8:679-98.

34. Candès EJ, Donoho DL. New tight frames of curvelets and optimal representations of objects with piecewise C2 singularities. Commun Pure Appl Math 2004;57:219-66.

35. Candès E, Demanet L, Donoho D, Ying L. Fast discrete curvelet transforms. Multiscale Model Simul 2006;5:861-99.